84

Under the microscope cover slip: spontaneous flows and bacterial behavior

L. Vincent and E. Kanso*

Department of Aerospace and Mechanical Engineering,
University of Southern California,
Los Angeles, 90089-1191, USA
*E-mail: Kanso@usc.edu
Kanso.usc.edu

Quantifying the dynamics of bacteria is a sinuous road with multiple challenges and subtleties. In this work, we take advantage of the natural evaporation-driven flow in a microscope sample to gain insight into the dynamics of motile bacteria in a unidirectional flow. We find that bacteria tend to align with or against the background flow. We also present in a didactic way every step of the study, with particular attention to explaining the cell tracking algorithm.

Keywords: Bacteria, tracking, rheotaxis

1. Introduction

The response of motile unicellular microorganisms to flows is believed to play a role in a large panel of biological processes. Example range from host-bacteria recruitment,[1] to biostreamers generation.[2,3] Indeed, the cells' response to various stimuli attracted considerable (and increasing) attention in the past few decades. Bacteria or algae have been shown to modify their behavior when exposed to cues such as chemical gradients,[4–6] light,[7,8] or gravity.[9] Recent contributions have identified that flows, or most specifically shear, can affect bacterial behavior as well: the various effects are grouped under the name "rheotaxis". In contrast to fish,[10,11] planktonic cells,[12,13] and copepods,[14] for which the ability to sense and actively respond to flows have been well identified, the cause of rheotaxis for bacteria is a current topic of discussion and seems to depends widely on the microorganism. Rheotaxis for prokariotes has initially been associated with the presence of surfaces. For instance, the upstream swimming of *Micoplasma Mobile*,[15] *E. Coli*[16] and *X. fastidiosa*[17] have all been observed close to surfaces. In a more recent contribution, Marcos *et al.*[18] noticed that the bacterium *P.*

haloplanktis when placed in vortices, have a tendency to align with streamlines far from the wall as well. In another study, Marcos et al.[19] observed shear-induced velocity in *B. subtilis*, that was interpreted as a result of the flagella shape; they emphasized that bacterial rheotaxis is very sensitive to change in morphology, so is likely to depends on species. Rusconi *et al.*[20] showed that flow alignment may interfere with swimming mechanism and lead to "trapping" in high-shear regions, for the two bacteria *B. subtilis* and *P. aeruginosa*. These studies explain such bacterial behavior as a direct consequence of their swimming mechanism and shape, and the possible interaction with a wall. They also point out the large variety of behavior, owing to the diversity in shape and swimming mechanism.

In this paper, we consider a simple experimental set-up involving a standard microscope slide with a drop of saliva water instilled in the middle and gently covered by a microscope cover slip. This set-up generates spontaneous, pump-less, and temporary flows, due to capillary and evaporation effects. To our best knowledge, these flows have been fairly undocumented although widely known to researchers looking at such systems. Capillary- and evaporation-driven flows are currently being explored as a way to pump fluid in microfluidic systems,[21,22] partially motivated by the direct analogy of these synthetic systems with fluid transport in plants.[23,24] However, the experimental set-up described here is not amenable to controllable and repeatable flow conditions. We therefore view this set-up as a pedagogical tool, which we use both to describe the imaging/tracking techniques for quantifying the motion of motile cell and to highlight interesting observations on the behavior of motile cells in externally-driven flows.
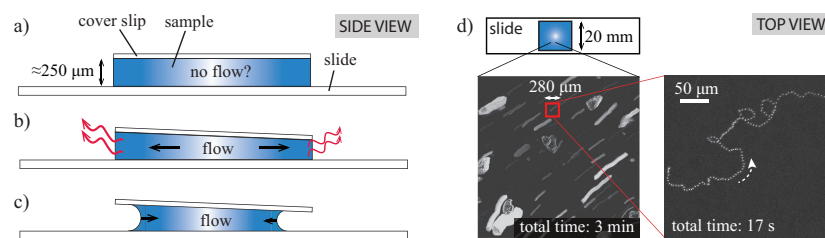

Fig. 1.   (a) Idealization and (b-c) real-life slide-sample-cover slip system: capillary action, evaporation, and contact line de-pinning generate micro-scale flows under in the liquid sample. (d) Flows are highlighted by the displacement of 50–200 μm Pliolite particle in the sample; they are locally uniform in space and time (up to several minutes) and persist as the sample dries. In this work, bacteria motion is characterized on shorter time scales and much smaller length scales.

86

In microbiology, tracking algorithms are applied to the study of motile micro-organisms, often as a way to probe their dynamics in response to a stimuli like chemical gradient or flow disturbances. Tracking algorithms have been gradually improved to work autonomously and track more objects and with more accuracy than a human operator, hence saving considerable time and effort while removing the uncertainty associated with a human operation. Tracking typically involves steps such as: detecting, characterizing, and following moving objects; each task presents its own challenges. For dilute suspensions, when the microorganisms can be tracked individually, traditional methods involve the use of Particle Tracking Velocimetry (PTV).[19,25,26] Typical difficulties for two-dimensional tracking of rigid objects include: partial occlusion, rotation, and overlapping; living cells may also exhibit change in size, shape (deformation), and duplication (e.g. as a result of cell division).[27] Additional difficulties arise from the imaging process itself: change in brightness (unsteady illumination), camera noise, lack of clarity; particularly, in phase-contrast microscopy bacteria can appear black or white depending on their relative position and orientation compared to the focal plane.[26,28] If the microorganisms are allowed to swim in three dimensions, that is to say in and out of the focal plane, the algorithm should also be able to deal with image blur and change of scale. Recent efforts opened to more sophisticated techniques such as holographic PTV,[29] allowing reconstruction of trajectories in three dimensions from a sequence of holograms recorded with a single camera; this turns to be especially useful to probe the complex kinematics of some swimmers.[30] Alternatively, rather than running the tracking software in post-processing, one can feed real-time information about the bacteria's position back into a high-speed motorized microscope stage: this allow tracking one bacteria for a quasi-unlimited period of times in two or even three dimensions.[31,32] For dense suspensions, following individual trajectories becomes illusory. However, the microorganisms themselves can act as seeding particles, therefore allowing the use of Particle Image Velocimetry (PIV) algorithms[33,34] (see, e.g., Ref. 35,36). PIV involves estimating the displacement and deformation, between two successive images, of interrogation windows containing large (10+) numbers of microorganisms, that are assumed to move in a locally coordinated fashion. Tracking algorithm complexity and efficiency has skyrocketed in the past 20 years. Yet, the building blocks of such scripts remain the same.

Our goal here is to present a fairly usable and robust tracking algorithm built on relatively simple ideas. The image processing and cell tracking al-

gorithm is described step-by-step in a didactic approach. The algorithm is validated using an example of a rising bubble with predictable dynamics. Finally, the algorithm is applied to the study of the behavior of a motile bacteria of the oral ecology swimming in two dimensions under the microscope cover slip. We show that these round-shaped vigorous bacteria swim preferentially upstream and downstream when exposed to unidirectional flows.

2. Experimental methods

Experimental set-up. Consider the simple manipulation, usually done in elementary courses in biology, involving a standard 75 x 25 mm microscope slide with a drop of water instilled in the middle. Now suppose a 22 x 22 mm cover slip is gently deposited on top of the drop. Due to the strong hydrophilic nature of (clean) glass, the drop flattens within seconds. The microscope slide and cover slip are now separated by a thin layer of water ($\sim 100~\mu$m), and to the naked eye no motion agitates this pool. Putting the sample under a microscope, one realizes that nothing is really still under the cover slip. Dust particles that have contaminated the water drop when preparing the sample are now seen to be advected by vigorous flows. In many experiments, it is desirable to prevent any exchange with air to prevent contamination, chemical gradients, or evaporation (cf., e.g., Ref. 35). Here we use the latter to our advantage, namely, to generate and examine these microfluidic flows. These flows originate from a combinations of factors, illustrated in Fig. 1. First, due to inhomogeneities in the initial drop position and spreading, the cover slip is unlikely to lay parallel to the slide, resulting in gravity-driven and capillary flows. Second, the water sample is not completely sealed: evaporation occurs at the sides resulting in mass transfer driving fluid from the center to the periphery of the sample (Fig. 1(b)), in a way analogous to the formation of the so-called "coffee-ring effect".[37,38] Another flow-driving effect, illustrated by Fig. 1(c), is the motion of the air-water interface under the cover slip: rather than being pinned to the cover slip edges, the contact line can occasionally move inward, therefore mechanically pushing the fluid ahead.

We probe the so-generated flows using a Nikon Ti-U microscope equipped with phase contrast optics, and a Nikon S Plan Fluor ELWD 40X/0.60 objective. Images are acquired with a high-resolution camera (Point Grey Grasshopper3, 2048×2048 pixels), at 40 fps; the corresponding working field of view is 280×280 μm. Looking through the 40X lens, the flow under the cover slip appears locally uniform in direction and strength
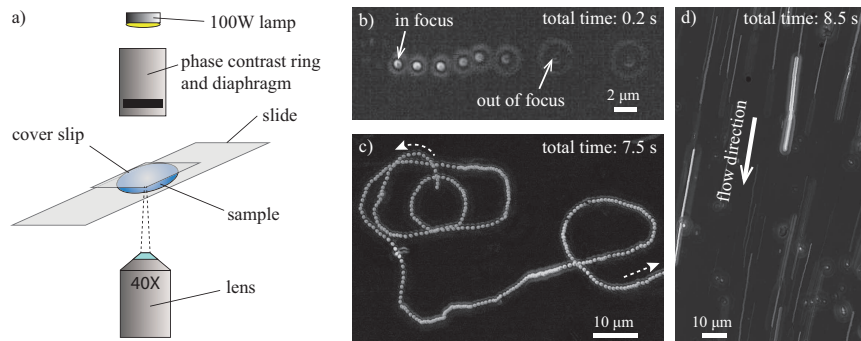
88

Fig. 2. The experimental sample is squeezed between a microscope slide and a cover slip, and placed on the stage of an inverted phase-contrast microscope. (b) The thickness of the sample initially allows the motile bacteria to swim in and out of the imaging plane; as the sample dries, the motion become two-dimensional (c), while locally steady uniform flows persist under the cover slip (d). Images (c) and (d) have been processed to highlight the moving objects (see Fig. 3).

(cf. Fig. 1(d)), with velocities typically ranging from 1 to 10 μm/s. The flow eventually changes direction, usually after several minutes.
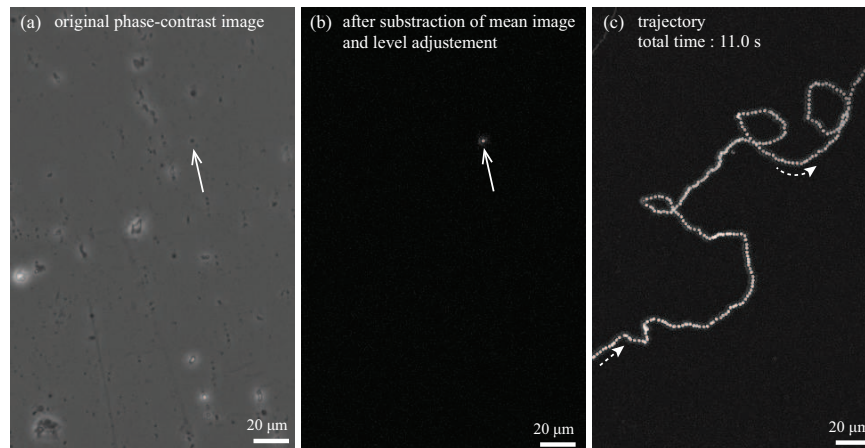

Fig. 3. Image pre-processing steps. Subtracting the median of all frames from the current frame (a) highlights the moving objects in the frame: (b). The solid arrow indicates the bacteria location in both images. Computing the maximum of (b) for all frames reveals the trajectory, which gives a *qualitative* idea of the bacteria's dynamics.

Samples of motile cells. Consider a drop of saliva following the same preparation described above. We examine the saliva sample using phase-constract microscopy, see Fig. 2(a). Microscopic images reveal motile cells that, in contrast to the passively-advected dust particles, move in a non-trivial way, showing frequent changes of velocity and curly trajectory, see Fig. 2(b-c). Note that cells are fairly transparent objects, making classical bright-field microscopy, which relies on light attenuation, fairly inadequate for proper observation. Phase-contrast microscopy, which highlights deflected optical paths, is a more suitable and commonly used method (cf., e.g., Ref. 19,26,28,39), since bacteria naturally induce a generous amount of refraction.

Images taken a few minutes after the sample preparation show few cells that frequently swim in and out of the focal plane, as shown in Fig. 2(b). Here, we focus on the cell behavior 20–30 min after the sample preparation: this ensures that motile cells are more numerous, albeit still in the dilute limit, and that they nicely stay in the focal plane, as evident in Fig. 2(c). Since the unsealed sample evaporates continuously, the spacing between the slide and cover slip decreases from its initial value of about 100–500 μm to about a few micrometers, making more objects visible in the thinner layer. Note that the thickness of the fluid layer is not known *a priori* but can be roughly estimated at time of observation. In Fig. 2(c), the motile cell stays in focus along the whole trajectory. According to Nikon data, a 40X lens with 0.60 numerical aperture has a depth of field of 1 μm; consequently, a completely focused trajectory takes place in a micrometer-thick plane plane, which means the motion is basically planar. Therefore, two-dimensional tracking gives a complete and accurate representation of its dynamics.

Image pre-processing. Using high-speed photography, our goal is to identify and track the behavior of motile cells. To this end, the raw phase-contrast images need to be turned into clean images suitable for automatic image processing and tracking. Image pre-processing consists of three basic steps: background identification, background subtraction and production of a chronophotography. In what follows, we illustrate these steps using ImageJ (or its extended version Fiji), a widely used open-source image processing software.[40,41]

Figure 3(a) shows a typical image recorded by the high-resolution camera. Clearly, a lot of objects are visible. To highlight the motile cells, one needs to remove all static objects from the raw image. This is accomplished

90

by first computing a representative image of the background and then subtracting it from all frames. For this step to work properly, special care needs to be taken during image capture; illumination, focus, and stage position should all remain unchanged during image acquisition. Vibrations and variations of any kind are undesirable, therefore it is best to use a low-noise imaging device. Note that some flaws can be partly compensated in pre-processing: for example, variation in light intensity can be compensated in Fiji with histogram-based bleaching (Image → Adjust → Bleach correction; method: Histogram Matching).

An image, or frame, is represented by a matrix, that is, by a set of values identifying the brightness of each pixel. A moving object induces a local change in brightness, i.e., in pixel value. A representative background image is composed of the most probable value of each pixel. One way to compute the background image is to take the average of each pixel across all frames (imageJ command: Image → Stack → Z projection → Average Intensity). A better albeit slower way, that reject intermittent changes such as a moving object passing by, is to calculate the median image MED (Image → Stack → Z projection → Median).

Given the background image MED, we can compute the difference between each individual frame and MED (Image → Process → Image Calculator → Operation: Difference). Figure 3(b) displays the result after level adjustments for one particular frame. The region of black pixels indicate no difference with MED; the brighter region indicates the presence of moving objects — here, a single moving object highlighted by the solid white arrow. Note that due to the phase-contrast technique, bacterial cells can appear both brighter and darker than the background,[26,28] therefore taking the *Difference* (i.e. absolute value) is always preferred to *Subtraction* (where negative values, corresponding to darker pixels on the original image, are set to zero). Lastly, to obtain a qualitative idea of the cell's trajectory, one could compute the maximum of the resulting images MAX (Image → Stack → Z projection → Max Intensity). Figure 3(c) shows the rich dynamics of a particular cell, which turns out to be very representative of the cell behavior observed in our experiments.

Tracking algorithm. The chronophotography in Fig. 3(c) provides a qualitative picture of the cell motion, but it does not give quantitative information about the kinematics. To this end, we developed a tracking script in MALTAB, able to follow the planar evolution of a bacterial cell.

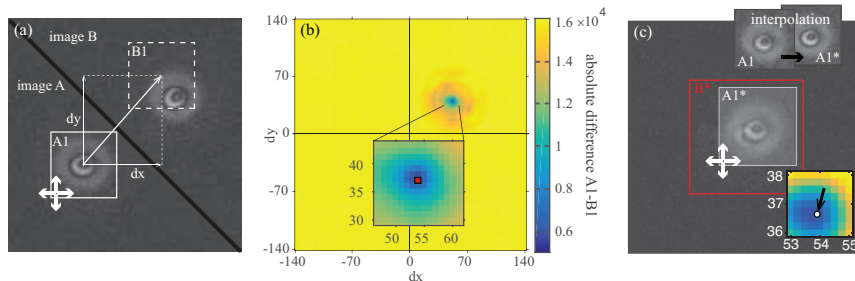Our script relies on the fact that the cell appearance changes slowly

Fig. 4.   Basic principle of the tracking script for each image pair A-B. (a) Scanning every possible displacement (dx,dy) within a pre-defined search area, the difference (L^2 norm) between the bacterium image A1 and the window B1 is computed. (c) The resulting map usually exhibit a clear minimum (thick arrow) corresponding to the most probable displacement with a 1-pixel precision. (c) Sub-pixel precision is achieved by repeating the process using interpolated images in a limited area around the previously estimated position (red square), and interpolating the minimum in the resulting map (white dot). dx, dy and dt are exaggerated in this illustration. The displacement is exaggerated for clarity.

between consecutive frames, even when significant changes in appearance and orientation are observed after hundreds of frames. Therefore, we take the cell position at time t, match its image at time t+dt, and deduce its displacement. This is a rudimentary form of image correlation, used for example in Particle Image Velocimetry (PIV).[33,34] Though we use it to track one motile object at a time, this algorithm differs from most of particle tracking velocimetry in the sense that it doesn't formally identify the object being tracked with characteristics such as brightness, histogram, shape, size, etc. It only assumes the object's image is slowly changing over time. Therefore it can deal naturally with changes in appearance such as those induced by defocusing (cf. Fig. 2), as long as they happen gradually.

The user needs to input three parameters: the size of the bounding box (completely encapsulating the moving objet), the maximum displacement of the moving object between frames, and the object's initial location. A chronophotography such as Fig. 3 allows the user to identify all three parameters and is displayed during the script initiation step. In the video sequences recorded for this study, the width of the bounding box is typically 15–30 pixels, and the maximum displacement between two consecutive frames in the image sequence (recorded at 40 frames per second) is of the order of one cell diameter, i.e., 5–10 pixels. Once these parameters are set, the processing is completely automatic.

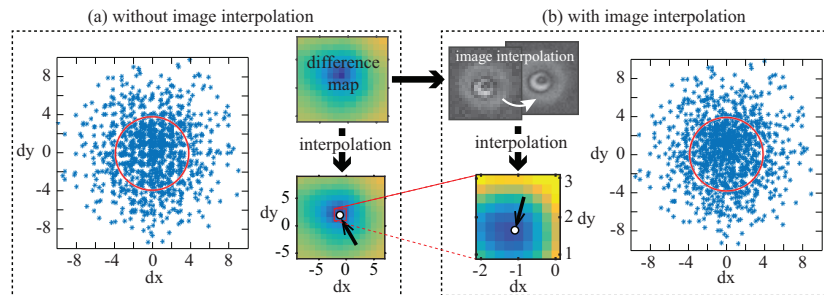Consider two images, image A at time t and image B at time t+dt, that

92

Fig. 5.   Benefits of image interpolation: scatter plots of raw displacement data (a) without and (b) with image interpolation , for a typical image sequence of N=1200 frames with no background flow. Bypassing image interpolation leads to "peak-locking", i.e. visible crumpling of data around integer displacements. Red circle shows average displacement defined as $1/N(\sum_{1 \rightarrow N} \sqrt{dx^2 + dy^2})$.

both display the cell. Assuming we know the cell's position at time t (in image A), the script first identifies a square image (interrogation window) using the user-defined box size that completely encapsulate the objet; this image is called A1. Through a scanning process, A1 is then compared to windows B1 of identical size extracted from image B, see Fig. 4(a); for all possible displacements (smaller than the user-defined maximum displacement), the absolute difference (in the L^2 norm) between A1 and B1 is stored. This process generates a map such as Fig. 4(b) where lower value means higher degree of similarity; this is analogous to cross-correlation maps generated by PIV algorithms.[34] The location (dx, dy) of the minimum indicates the most probable displacement of the cell between A and B, with a precision of 1 pixel. We then refine this initial estimate to sub-pixel precision. To this end, the mapping process is repeated in a limited area around the displacement previously estimated, but this time using images interpolated to 4 times their original x and y resolution. This leads to a secondary difference map Fig. 4(c), from where the interpolated location gives the final displacement estimation. It is worth noting that with our experimental images, interpolating images more than 4 times in x and y only provided limited benefits, and wasn't worth the necessary decrease in processing speed.

Is image interpolation really necessary? One might be tempted to bypass image interpolation for speed and simplicity, and directly locate the minimum in the original difference map with the best precision possible. These results are shown in Fig. 5(a): instead of being homogeneously distributed, the data shows a grid-like pattern (especially visible inside red circle). That

is the data is biased towards integer displacements. This discretization artifact is known as "peak-locking" in PIV;[42,43] image interpolation is the most straightforward way of dealing with this issue. The displacement data evaluated using image interpolation is displayed in Fig. 5(b).

Finally, note that a direct comparison between the actual and reconstructed image sequences shows that the reconstruction algorithm performs very well in terms of both robustness and speed. Here, we used one core of a 3-year old Mac Pro desktop computer. The processing speed was around 10 image pairs per second in common conditions with full resolution images (4 Mpix), and around 40 images pairs per second with downsampled images (1 Mpix) — the image reading process takes a comparable time to the algorithm itself. It technically means that the script could be used for real-time tracking.

Limits and potential improvements. The error in the cell displacement estimated at each time step depends on many factors, such as the size of the interrogation window, the image clarity, and more importantly how well the object in image A compares with the one in image B. Accumulated error may lead to inaccurate estimates of the cell motion, or worse, may cause the script to loose track of the object. One way to workaround this is to "re-center" the tracking window regularly, by repeating at various intervals the comparison process with the first image of the sequence. In practice, a good focused image such as Fig. 4(a) does not induce significant accumulated error, i.e. less than 5 pixels after 500 iterations, and no "re-centering" is needed.

This script as presented here performed satisfactorily for all image sequences acquired for this study. However, one must be cautious when using it more generally. This script relies on the fact that the object in image B is fairly similar to the object in image A. While this turned out to be a reliable criterion, it may fail in situations such as (i) sudden change in brightness, (ii) sudden masking, (iii) significant rotation of non-axisymmetric objects. The latter can be resolved by adding rotational degrees of freedom to the reference object image (A1). However, addressing (i) and (ii) requires more complex image processing. One possible improvement, as noted previously, is to use FFT-based correlation (such as phase correlation) rather than image difference: sensitivity to noise, and to a smaller extent, brightness and partial masking are likely to be reduced. Another possible improvement is use the Kalman filter to improve the signal/noise ratio of the past trajectory and provide an estimation of future positions. This method, however,

94

may have limited benefits, given the fairly unpredictable dynamics of the bacterial cells.
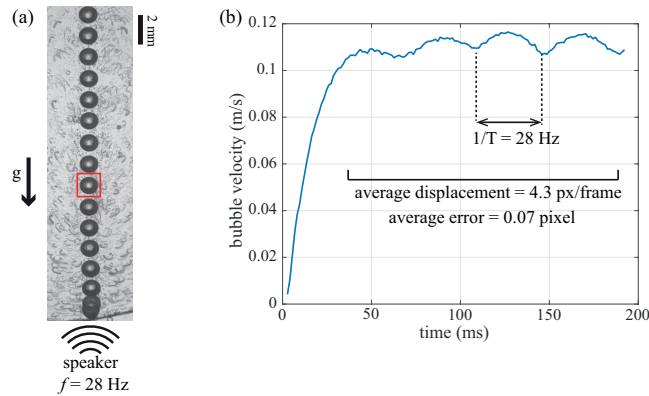

Fig. 6.   Tracking script validation with a round object with predictable dynamics: (a) a millimetric bubble is rising under buoyancy in a Hele–Shaw cell with added background acoustic vibration. Video was recorded at 700 fps (1 every 10 images displayed). Red box shows the tracking window used by the algorithm. (b) The tracking script accurately reproduces the bubble's motion, including sub-pixel background vibration.

Validation of the tracking algorithm. To test the script, we used a simple system consisting of millimeter-scale bubble rising under buoyancy in a Hele–Shaw cell filled with water, see Fig. 6(a). The spacing between the front and back plexiglass walls is 1.0 mm. As an additional layer of complexity, a speaker oscillate the cell vertically at a frequency $f = 28$Hz, with a sub-pixel amplitude. The fluid is seeded with 200-μm PIV particles as a way to introduce interferences in the image comparison process. The movie is recorded with a Phantom M-110 high-speed camera equipped with a micro-Nikkor 60 mm; the frame rate is set to 700 fps.

The resulting velocity, as estimated by the tracking script, is shown in Fig. 6(b). As expected, the bubble rises monotonically and ultimately oscillates around a terminal velocity value of 112 ± 3 mm.s^{-1}. We now provide a theoretical estimate of the terminal velocity of the bubble. The terminal Reynolds number $\mathrm{Re} = \rho D V_t / \eta$ of the rising bubble is equal to 150. Here, D and V_t are respectively the bubble diameter and terminal velocity, and ρ and η are the density and dynamic viscosity of water. The drag coefficient of the sphere, assumed to be solid, smooth and unconfined, is given by $C_x \sim 0.80 \pm 0.05$ (cf., e.g., Ref. 44, p.181). Balancing inertial

drag $1/8C_x\rho\pi D^2 V_t^2$ with gravity-corrected buoyancy $4/24(\rho - \rho_{air})\pi D^3 g$ yields the terminal rising velocity:

$$V_t = \sqrt{\frac{4}{3}\frac{gD(\rho - \rho_{air})}{\rho\,C_x}} \simeq \frac{2}{\sqrt{3}}\sqrt{\frac{gD}{C_x}} \tag{1}$$

Given $g = 9.81$ m.s^{-2} and $D = 1.30 \pm 0.03$ mm, we find $V_t = 140 \pm 10$ mm.s^{-1}, which is a slight overestimation of the observed value 112 ± 3 mm.s^{-1}. The discrepancy is possibly owing to the presence of walls, which is not consistent with the assumption of unconfined bubble. More importantly, the estimated velocity reflects faithfully the imposed sub-pixel vibration; we calculated that the velocity was estimated with an error of 2 mm.s^{-1}, i.e. 0.05 pixel / frame, comparable to PIV with similar window sizes.[34]

Furthermore, to better realize the benefit of using grayscale images over binary images (that usually result from thresholding grayscale images), one can compare the estimated accuracy reported above to the one obtained using a home-made centroid-based tracking algorithm that rely on blob detection via thresholding (not detailed here for brevity). We compare the two using the same image sequence shown in Fig. 6, which is characterized by a high contrast between the bubble and the background, and thus particularly suitable for thresholding. The accuracy of the centroid-based algorithm is estimated to be 0.3 px, roughly 8 times the accuracy of our image-comparison based script. The validation study emphasizes that the script is not limited to bacterial cells: it performs well for any round objet (or not-rotating bluff body), even in a fuzzy environment.

3. Confined bacterial cells in slow background flows

We now observe and characterize the dynamics of a single bacterial cell in 25 individual experiments. The image sequences obtained in each case are analyzed using the tracking algorithm described above. Further, the direction and velocity of the background flow are also computed to gauge the influence of the background flow on the bacterial motion.

The cases considered here are extremely dilute, where at most two or three bacterial cells are simultaneously present in the frame. There is no swarming or collective dynamics, as described for example in Ref. 35,36,45. The bacteria are observed to swim in two dimensions, i.e. they do not swim out of the focal plane. Hence the two-dimensional tracking provides a faithful representation of the dynamics. The visualization window, 280 $\times$ 280 μm at 40X magnification, is fixed and the movie is recorded until
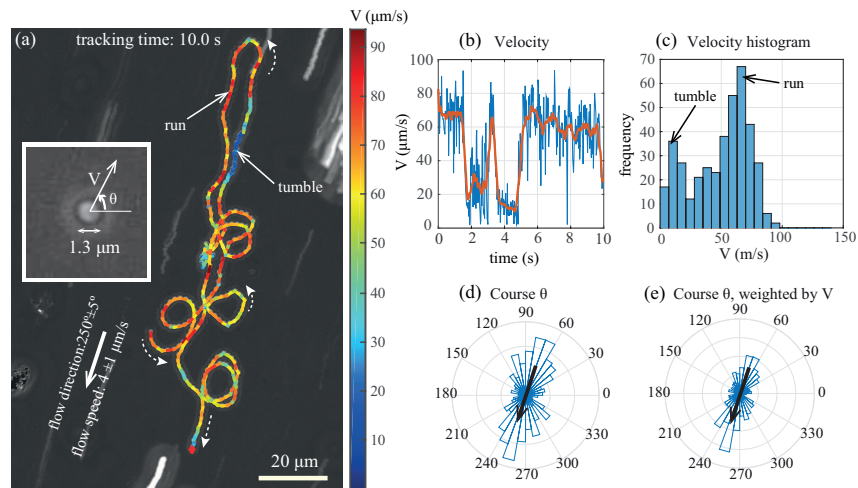
96

Fig. 7.   Representative example of bacteria dynamics, after tracking. (a) Overview of the trajectory; passive tracers in the background highlight the flow direction.(b) The bacterium swim with a fairly erratic velocity (blue: raw velocity data, red: moving average) but preferentially swim at two well-defined velocity (c), and frequently align with the flow direction (d). Aligned trajectory segments correlate with high velocity, as shown by narrower speed-weighted distribution (e): the bacterium is not passively advected by the flow but deliberately swim with or against the flow. Thick black arrows shows the flow direction in the roses (d)-(e). Loops are mostly executed counter-clockwise. Uncertainty on velocity is 2 μm/s (0.4 pixel)

the bacterium leaves the frame. Recording durations of individual trajectories typically range from 10 to 30 seconds, during which we observed no significant change in the background flow (magnitude or direction). The background flow magnitude is typically within 2–10 μm/s, thus one order of magnitude smaller than the bacterium's top velocity (50 - 80 μm/s).

A typical cell behavior is shown in Fig. 7. This figure corresponds to a 10-second (400 frames) video sequence showing the full trajectory of a bacterium (no interruption). As obvious from Fig. 7(a-b), the bacterium's velocity appears to be fairly intermittent. However, a closer look reveals that the bacterium swims preferentially at two velocities (indicated by thin black arrows in Fig. 7(c)). The fast velocity, around 60 μm/s corresponds to "free" swimming events with slow changes of direction over time; we call these phases 'run', even though their is a significant variation of the swimming velocity during these phases. The slow velocity, around 10 μm/s, corresponds to phases of more erratic motion with frequent changes of swimming direction and orientation; visually, the bacteria appears to be "shaking".

The double-peaked speed histogram (c) proved to be typical of all recorded trajectories.

Another notable feature of the dynamics is the consistent alignment with the background flow, shown by the course histogram (Fig. 7(d)). One could interpret this general alignment as a result of passive advection by the background flow. However, this intuitive idea is essentially wrong for two reasons. First, the bacterium goes against the flow as well as *with* the flow with equal probability. Second, good alignment correlates to high cell velocities, which values range from 5 to 10 times that of the background velocity. One way to highlight this is to weight the course distribution histogram by velocity: the distribution narrows even more closer to the flow direction (Fig. 7(e)). As a consequence of these observations, we can safely deduce that the bacterium actively swims upstream or downstream, rather than at any other orientation. The dynamics is also marked by low-speed swimming or "tumble" events (centered around 10 μm/s) when the bacterium changes orientation. During these events, the bacterium velocity is comparable to the background flow and the bacterial cell re-orients upstream or downstream, as shown in Fig. 7. This supports the claim that the re-orientation events are dynamically biased, rather than disorganized in an isotropic way.

Lastly, one can notice the bacterium execute frequents loops, a vast majority of them being counterclockwise, and displaying curvature radius of the order of 8 mm. These are reminiscent of the circular trajectories adopted by E. coli near a glass surface, observed by several authors[4,46] and explained by Lauga et al.[47] This peculiar motion is thought to be a result of the bacteria's swimming mechanism interacting with a flat solid boundary; this may suggest that the bacteria we observe are swimming close to the glass slide or cover slip, either deliberately, or as the result of strong confinement in the vertical direction.

One can legitimately wonder about the generality of the behavior reported in Fig 7. Specifically, are (i) the velocity patterns and (ii) the alignment with background flow typical behavior under these experimental conditions? Figure 8 shows the data sets collected under two different experimental conditions corresponding to background flows of different directions but comparable speed. Under each experimental condition, six individual cell trajectories are reported. The results are combined to produce a single stitched trajectory and a single velocity histogram. Obviously the cell behaviors reported in Figs. 8(a) and (b) are dissimilar in a number of ways: trajectories in (a) show frequent loops and are highly intertwined, while
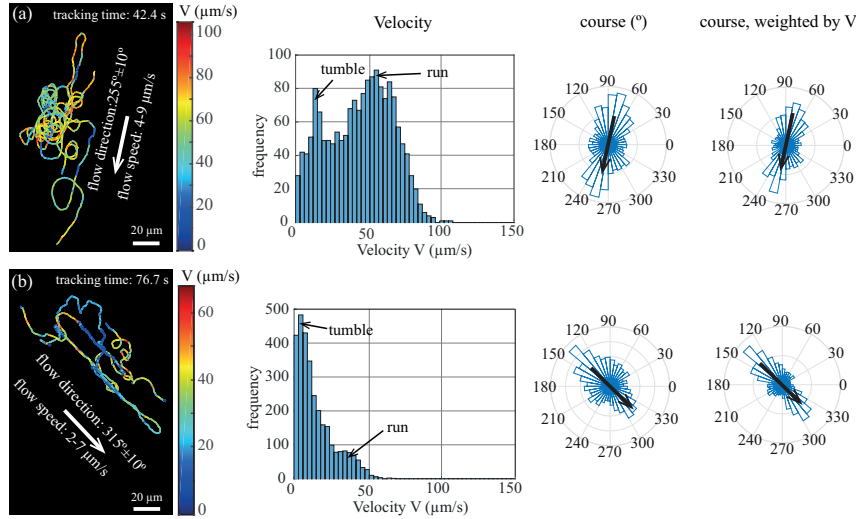
98

Fig. 8.   Combined trajectories for similar background flow, showing various velocity patterns but consistent alignment with the background flow. (a) shows a similar pattern than Fig 7, characterized with a predominance of "run" velocity in a gaussian-like way, and a sharp low-velocity peak. (b) shows mostly low velocity events, though a "run" peak can still be discerned in the distribution tail. In both cases, there is still a clear alignment with the background flow, which narrows when weighted by velocity, highlighting the bacteria's free will. Thick black and white arrows show the flow direction.

trajectories in (b) show longer and straighter path; bacteria in (a) are more inclined to swim at their cruise speed (around 50–55 μm/s), while bacteria in (b) preferentially swim very slowly (5 μm/s), adopting occasionally a somewhat smaller cruise speed (35 μm/s). Yet, despite these differences, some similarities persist. First, the double-peaked velocity pattern can clearly be distinguished in both data sets. Second, and more importantly, most displacements are again sensibly aligned with the flow direction, with equi-distribution between upstream and downstream displacements; again, weighting the data with velocity narrows the distribution even further along the flow direction, suggesting that alignment with and against the background flow is a typical behavior.

One could describe this dynamics in terms of a biased diffusion process. To this end, we compute the mean square displacement (MSD) projected along the directions parallel and transverse to the flow. Fig. 9 shows the MSD for the data shown in Fig. 8(b). It is clear that the MSD along the flow direction is much more efficient than MSD along the transverse direction – in fact, the two MSDs are several orders of magnitude apart. Note that, for
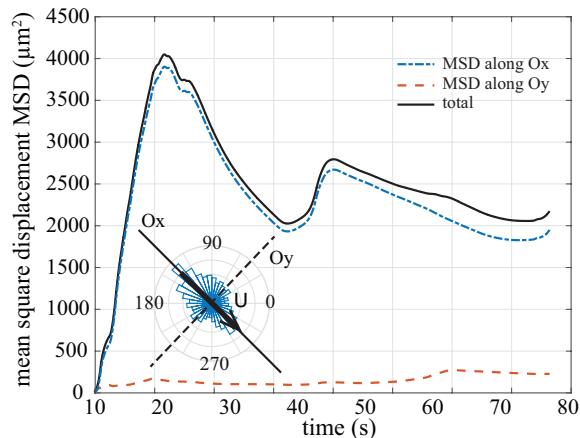
Fig. 9.   Total mean square displacement (solid lines), and components along the background flow axis Ox (dash-dotted line) and along the orthogonal direction Oy (dashed line), for the data of Fig. 8(b). The diffusion along the background flow axis is about one order of magnitude more effective.

free swimming bacteria exhibiting run-and-tumble behaviour, one expects the MSD to be linear in time for $t >> 1$, with the slope being the diffusion coefficient. Here, we do not observe such linear relationship, and thus cannot extract accurate values of the parallel and transverse diffusion coefficients. One reason may be due to the fact that our data set is relatively small; we leave this endeavor of collecting more data points for future work.

We conclude this section by noting that there are a number of ways by which one can improve the quality of the flow in this basic setup. For instance, by using a long cover slip and applying sealant on the long edges, one gets a rudimentary evaporation-driven channel. Further, exposing one of the open ends to moist air, one could make the flow unidirectional and reduce or even eliminate drying, thus allowing substantially larger observation time.

4. Conclusions

We used a tracking algorithm based on image-comparison to probe the two-dimensional dynamics of fast-swimming bacteria of the oral ecology under the microscope cover slip. We observed capillarity and evaporation-driven transitory flows spontaneously occurring under the cover slip of a traditionally-prepared "slide-sample-cover slip" sandwich. When observed at the right length scale (< 1 mm) and time scale (< 1–5 min), these tran-

100

sitory and fairly undocumented flows are practically uniform and constant, with speed typically ranging from 1 to 10 μm/s. We took advantage of these flows to expose a fast-swimming bacterium to unidirectional flows weaker than its own swimming velocity.

We detailed the way image acquired with a phase-contrast microscope and a high-resolution camera can be prepared for automatic analysis. Then we explained the building blocks of a minimal sub-pixel tracking script based on pattern matching between image pairs, tested on a round moving object with predictable dynamics. The script performed remarkably well, with resolution less than 0.1 pixel for a 40-pixel wide interrogation window, and never failed to track the motile bacteria in all the image sequences acquired for this study.

Bacteria trajectories in weak background flows under the microscope cover slip displayed the following characteristic patterns. The bacterial cells preferentially swim at two velocities: a fast velocity corresponding to "running" segments with slowly-changing course and a slow velocity, associated to long-lasting tumble-like events. The observed tumbling differ from tumble usually reported in the literature in the sense that (i) they can last several seconds and (ii) the bacterium generally keeps the swimming direction it had before the "tumbling" event; yet, during these events, the bacterium frequently rotates and appears to be "shaking". When swimming at their cruise speed, bacteria were generally found to align with the background flow, going upstream as well as downstream with nearly equal probability. The swimming speed, usually up to one order of magnitude higher than the background flow velocity, suggests that this alignment is not the result of passive advection, but is some form of bacterial rheotaxis.[19] This observation is in contrast to positive (aligning with the flow) or negative (aligning opposite to the flow) rheotaxis traditionally reported in the literature, in the sense that microorganisms usually display one or the other, but not both at the same time as observed here. In a somewhat less quantifiable manner, slow swimming and tumble-like events also show alignment with the flow direction. We note that the mean square displacement is several orders of magnitude greater in the direction parallel to the background flow than in the transverse direction, suggesting a biased diffusion behaviour. In future experiments, we will collect enough data to be able to reliably measure the diffusion coefficients along each direction. We also note that the occurrence of circular trajectories, reminiscent of what has been observed for pushers such as E. coli close to solid boundaries, suggesting the observed dynamics are the result of the interaction with the glass slide or cover slip,

and possibly shear.

To conclude, we highlight that theoretical models of microswimmers strongly confined in a thin liquid film, with the dimension of the swimmers being comparable to the thickness of the fluid film, have been recently considered in a number of studies.[48–50] Confined microswimmers have a distinct hydrodynamic signature in the sense that the far-field flow generated by the swimmer is that of a 2D *potential source*. The dipolar far-field is independent of the swimming mechanism and is rooted in the fact that the basic physics in confined fluids is that of a *Hele–Shaw* flow.[51] Further, due to friction with the nearby walls, confined microswimmers with geometric asymmetry (large head or large tail) reorient in response to the local background flow, by orienting either in the local flow (large tail or vigorously beating flagella) or opposite to the local flow (large head or weakly beating flagella). The findings reported in this study seem to agree broadly with the theoretical predictions. However, a detailed look at these cells' flagellar activity and whether it is responsible for the alignment with or against the background flow remains an open question. We will address these issues more rigorously in future studies. To this end, we will first identify the bacterial type or opt to use a bacterial model system such as *E. Coli*. We will also control the viscous or viscoelastic properties of the fluid environment, as well as the speed and direction of background flow using a microfluidic pump.

References

1. M. J. McFall-Ngai, The importance of microbes in animal development: lessons from the squid-vibrio symbiosis, *Annu. Rev. Microbiol.* **68**, 177 (2014).
2. S. Yazdi and A. M. Ardekani, Bacterial aggregation and biofilm formation in a bacterial aggregation and biofilm formation in a vortical flow, *Biomicrofluidics* **6**, p. 044114 (2012).
3. M. K. Kim, K. Drescher, O. S. Pak, B. L. Bassler and H. A. Stone, Filaments in curved streamlines: rapid formation of staphylococcus aureus biofilm streamers, *New J. Phys.* **16**, p. 065024 (2014).
4. H. C. Berg and L. Turner, Chemotaxis of bacteria in glass capillary arrays. escherichia coli, motility, microchannel plate, and light scattering., *Biophys. J.* **58**, 919 (1990).
5. R. Stocker, J. R. Seymour, A. Samadani, D. E. Hunt and M. F. Polz, Rapid chemotactic response enables marine bacteria to exploit ephemeral microscale nutrient patches, *PNAS* **105**, 4209 (2008).
6. R. Stocker and J. R. Seymour, Ecology and physics of bacterial chemotaxis in the ocean, *Microbiol. Mol. Biol. Rev.* **76**, 792 (2012).
7. L. Ragatz, Z.-Y. Jiang, C. E. Bauer and H. Gest, Macroscopic phototactic

102

behavior of the purple photosynthetic bacterium *Rhodospirillum centenum*, *Arch. Microbiol.* **163**, 1 (1995).

8. J. P. Armitage and K. J. Hellingwerf, Light-induced behavioral responses ('phototaxis') in prokaryotes, *Photosynth. Res.* **76**, 145 (2003).

9. T. J. Pedley, N. A. Hill and J. O. Kessler, The growth of bioconvection patterns in a uniform suspension of gyrotactic micro-organisms, *J. Fluid. Mech.* **195**, 223 (1988).

10. G. P. Arnold, Rheotropism in fishes, *Biol. Rev.* **49**, 515 (1974).

11. J. C. Montgomery, C. F. Baker and A. G. Carton, The lateral line can mediate rheotaxis in fish, *Nature* **389**, 960 (1997).

12. H. H. Jakobsen, Escape response of planktonic protists to fluid mechanical signals, *Mar. Ecol. Prog. Ser.* **214**, 67 (2001).

13. A. W. Visser, Hydromechanical signals in the plankton, *Mar. Ecol. Prog. Ser.* **222**, 1 (2001).

14. J. R. Strickler and A. K. Bal, Setae of the first antennae of the copepod cyclops scutifer (sars): Their structure and importance, *Proc. Nat. Acad. Sci. USA* **70**, 2656 (1973).

15. R. Rosengarten, A. Klein-Struckmeier and H. Kirchhoff, Rheotactic behavior of a gliding mycoplasma, *J. Bacteriol.* **170**, 989 (1988).

16. J. Hill, O. Kalkanci, J. L. McMurry and H. Koser, Hydrodynamic surface interactions enable escherichia coli to seek efficient routes ?to swim upstream, *Phys. Rev. Lett.* **98**, p. 068101 (2007).

17. Y. Meng, Y. L., C. D. Galvani, G. Hao, J. N. Turner, T. J. Burr and H. C. Hoch, Upstream migration of *Xylella fastidiosa* via pilus-driven twitching motility?, *J. Bacteriol.* **187**, 5560 (2005).

18. Marcos and R. Stocker, Microorganisms in vortices: a microfluidic setup, *Limmol. Oceanogr.: Methods* **4**, 392 (2006).

19. Marcos, H. C. Fu, T. R. Powers and R. Stocker, Bacterial rheotaxis, *PNAS* **109**, 4780 (2012).

20. R. Rusconi, J. S. Guasto and R. Stocker, Bacterial transport suppressed by fluid shear, *Nature Phys.* **10**, 212 (2014).

21. N. Goedecke, J. Eijkel and A. Manz, ??evaporation driven pumping for chromatography application, *Lab Chip* **2**, 219 (2002).

22. N. S. Lynn and D. S. Dandy, Passive microfluidic pumping using coupled capillary/evaporation effects, *Lab Chip* **9**, 3422 (2009).

23. X. Noblin, L. Mahadevan, I. A. Coomaraswamy, D. A. Weitz, N. M. Holbrook and M. A. Zwieniecki, Optimal vein density in artificial and real leaves, *PNAS* **105**, 9140 (2008).

24. A. D. Stroock, V. V. Pagay, M. A. Zwieniecki and N. M. Holbrook, The physicochemical hydrodynamics of vascular plants, *Annu. Rev. Fluid Mech.* **46**, 615 (2014).

25. A. A. Chengala, M. Hondzo, D. Troolin and P. A. Lefebvre, Kinetic responses of *Dunaliella* in moving fluids, *Biotechnol. Bioeng.* **107**, 65 (2010).

26. J. Xie, S. Khan and M. Shah, Automatic tracking of escherichia coli in phase-contrast microscopy video, *Biomedical Engineering, IEEE Transactions on* **56**, 390 (2009).

27. O. Debeir, P. V. Ham, R. Kiss and C. Decaestecker, Tracking of migrating cells under phase-contrast video microscopy with combined mean-shift processes, *IEEE Trans. Med. Imaging* **24**, 697 (2005).
28. L. H. Cisneros, J. O. Kessler, S. Ganguly and R. E. Goldstein, Dynamics of swimming bacteria: Transition to directional order at high concentration, *Phys. Rev. E* **83**, p. 061907 (2011).
29. J. Sheng, E. Malkiel and J. Katz, Digital holographic microscope for measuring three-dimensional particle distributions and motions, *Appl. Opt.* **45**, 3893 (2006).
30. J. Sheng, E. Malkiel, J. Katz, J. Adolf, R. Belas and A. R. Place, Digital holographic microscopy reveals prey-induced changes in swimming behavior of predatory dinoflagellates, *PNAS* **104**, 17512 (2007).
31. H. C. Berg, The tracking microscope, *Adv. Opt. Electron Microsc* **7** (1978).
32. P. Frymier, R. M. Ford, H. C. Berg and P. T. Cummings, Three-dimensional tracking of motile bacteria near a solid planar surface, *PNAS* **92**, 6195 (1995).
33. M. Raffel, C. E. Willert and J. Kompenhans, *Particle image velocimetry: a practical guide* (Springer, 2013).
34. C. E. Willert and M. Gharib, Digital particle image velocimetry, *Exp. Fluids* **10**, 181 (1991).
35. H. Wioland, F. G. Woodhouse, J. Dunkel, J. O. Kessler and R. E. Goldstein, Confinement stabilizes a bacterial suspension into a spiral vortex, *Phys. Rev. Lett.* **110**, p. 268102(5) (2013).
36. L. H. Cisneros, R. Cortez, S. J. DeCamp, C. Dombrowski, R. E. Goldstein and J. O. Kessler, Fluid dynamics of self-propelled microorganisms, from individuals to concentrated populations, *Exp. Fluids* **43** (2007).
37. R. D. Deegan, O. Bakajin, T. F. Dupont, G. Huber, S. R. Nagel and T. A. Witten, Capillary flow as the cause of ring stains from dried liquid drops, *Nature* **389**, 827 (1997).
38. P. J. Yunker, T. Still, M. A. Lohr and A. G. Yodh, Suppression of the coffee-ring effect by shape-dependent capillary interactions, *Nature* **476**, 308 (2011).
39. C.-K. Tung, F. Ardon, A. Roy, D. L. Koch, S. S. Suarez and M. Wu, Emergence of upstream swimming via a hydrodynamic transition, *Phys. Rev. Lett.* **114**, p. 108102 (2015).
40. W. S. Rasband, *ImageJ*. U. S. National Institutes of Health, Bethesda, Maryland, USA (http://imagej.nih.gov/ij/, 1997-2015).
41. C. A. Schneider, W. S. Rasband and K. W. Eliceiri, Nih image to imageJ: 25 years of image analysis, *Nature Methods* **9**, 671 (2012).
42. J. Chen and J. Katz, Elimination of peak-locking error in piv analysis using the correlation mapping method, *Meas. Sci. Technol.* **16**, 1605 (2005).
43. L. Gui and S. T. Wereley, A correlation-based continuous window-shift technique to reduce the peak-locking effect in digital piv image evaluation, *Exp. Fluids* **32**, 506 (2002).
44. L. D. Landau and E. M. Lifschitz, *Fluid Mechanics* (Pergamon Press, Oxford, 1987).
45. A. Sokolov, I. S. Aranson, J. O. Kessler and R. E. Goldstein, Concentration dependence of the collective dynamics of swimming bacteria, *Phys. Rev. Lett.*

104

98, p. 158102 (2007).

46. M. A. S. Vigeant and R. M. Ford, Interactions between motile *Escherichia coli* and glass in media with various ionic strengths, as observed with a three-dimensional-tracking microscope, *Appl. Environ.* **63**, 3474 (1997).

47. E. Lauga, W. R. DiLuzio, G. M. Whitesides and H. A. Stone, Swimming in circles: Motion of bacteria near solid boundaries, *Biophys. J.* **90**, 400 (2006).

48. N. Desreumaux, N. Florent, E. Lauga and D. Bartolo, Active and driven hydrodynamic crystals, *Euro. Phys. J. E* **35**, 1 (2012).

49. A. Lefauve and D. Santillan, Globally aligned states and hydrodynamic traffic jams in confined suspensions of active asymmetric particles, *Phys. Rev. E* **89**, p. 021002 (2014).

50. A. C. H. Tsang and E. Kanso, Flagella-induced transitions in the collective behavior of confined microswimmers, *Phys. Rev. E* **90**, p. 021001(R) (2014).

51. T. Beatus, The physics of 2D microfluidic droplet ensembles, *Phys. Rep.* **516**, 103 (2012).